

SCALAR TRANSPORT IN FLOW PAST FINITE CIRCULAR PATCHES OF TALL ROUGHNESS

D.D. Wangsawijaya¹, C. Nicolai¹, B. Ganapathisubramani¹

¹Aerodynamics and Fluid Mechanics Research Group, Faculty of Engineering and Physical Sciences
University of Southampton SO17 1BJ, United Kingdom
D.D.Wangsawijaya@soton.ac.uk

ABSTRACT

Simultaneous particle image velocimetry-planar laser-induced fluorescence (PIV-PLIF) measurements are conducted of the flow around and downstream of patches of tall cylinders with various solidity $\phi \equiv N_c(d/D)^2$, where N_c is the number of cylinders in a patch, d and D are the diameters of the cylinder and the patch, respectively. Results suggest that the bleeding and scalar concentration in the wake and above the patches are dependent upon ϕ . Recirculation bubble appears at the trailing edge (TE) of the patch, limiting the flow from convecting downstream and forcing the flow (and the scalar) to escape vertically from the top of the patch. Above the wake, a shear layer generated by the velocity difference shields the near-wake region. The net effect is the appearance of an elongated patch as ϕ decreases and a taller patch as ϕ increases. In terms of scalar transport, both advective and turbulent vertical scalar transport are enhanced as ϕ increases. High advective vertical scalar transport CV is concentrated around the canopy (above the canopy due to vertical bleeding and at the TE due to high scalar concentration), while high turbulent transport $\overline{c'v'}$ largely coincides with the shear layer. Joint probability density function (PDF) calculated at few selected points show that there is an entrainment of turbulent flows from the shear layer towards the wake of the patch below this layer, followed by scalar diffusion the the same direction and further downstream of the patch.

INTRODUCTION

A scenario where a developing turbulent boundary layer impinges a canopy is commonly found in both nature and engineering applications. Example includes: flows past aquatic and terrestrial vegetations, atmospheric boundary layer (ABL) developing over forests, urban landscapes, and wind/tidal turbines. The presence of these canopies are known to affect the scalar, momentum, and energy transport process in the flows, which in turn can affect the ecosystem surrounding the canopies. Here, the canopy is simplified as a group of tall cylinders of height h mounted on a circular patch (figure 1a), forming a porous body. Previous studies involved 2-D patches, where h is equal to or taller than the flow depth, serving as models for emergent aquatic vegetations (Nicolle & Eames, 2011; Chang & Constantinescu, 2015). A more realistic approach for vegetation canopies, urban landscapes, and wind farms is to submerge the patches in the flows ($h < \delta_{bl}$, see figure 1a). Studies on 3-D (submerged) patches have shown that solidity (or solid volume fraction) of a porous body ϕ is critical in the determination of drag and wake characteristics at the

TE of the patch (Taddei *et al.*, 2016; Nicolai *et al.*, 2020). Due to porosity, the flow may escape from the body by means of lateral, TE, and vertical bleeding, as illustrated in figure 1(a).

In this study, scalar measurements (PLIF) are conducted simultaneously with velocity measurements (PIV), allowing us to examine the instantaneous scalar fields as well as the velocity fields. We aim to investigate the characteristics of flow and scalar transport in the wake and above porous patches of as a function of patch density ϕ , given a point source of passive scalar upstream of the patch (figure 1a). As the scalar is released from the floor level, we particularly focus on the vertical scalar transport by the time-averaged (advective) and the fluctuating turbulent components of the flow, as these parameters characterise mixing on the flow downstream of the porous patches. As a comparison, the range of ϕ in this study is within the typical range observed for aquatic vegetations and urban areas (Grimmond & Oke, 1999; Nepf, 2012). The height of cylinders, when compared to ABL ($h/\delta_{bl} = 0.366$), is typical of tall buildings in the cities.

EXPERIMENTAL SETUP

Simultaneous PIV-PLIF measurements are carried out in the closed loop water flume at the University of Southampton. The test section has the size of 6250 mm \times 1200 mm (length \times width), filled with water whose level is kept constant at 600 mm. A circular patch ($D = 100$ mm and $Re_D \equiv U_\infty D/\nu \approx 4.5 \times 10^4$, where $\nu = 1.0035 \times 10^{-6}$ m²s⁻¹ is the kinematic viscosity of water at 20°) is mounted on the floor of the tunnel at 5500 mm downstream of the test section entrance. The incoming flow is a developing turbulent boundary layer, whose freestream velocity $U_\infty \approx 0.45$ ms⁻¹ and boundary-layer thickness $\delta_{bl} = 82 \pm 3$ mm ($Re_\tau \equiv \delta_{bl} U_\tau/\nu \approx 1500$ and $Re_\theta \equiv \theta U_\infty/\nu \approx 3000$, where U_τ is the friction velocity, and θ is the momentum thickness). A point source is created at 1.25D upstream from the centre of the patch by releasing Rhodamine 6G dye solution (Peclet number $Pe_D \equiv Re_D Sc = 1.12 \times 10^8$, where Sc is the Schmidt number) from the ground level at a constant flow rate (figure 1a).

Mounted on the circular patch are rigid cylinders made of photopolymer resin ($d = 5$ mm, $h = 30$ mm). The cylinders are arranged in a manner pictured in figure 1(b–d), such that ϕ is parametrically varied by increasing N_c while keeping D and d constant. Table 1 and figure 1(b–e) illustrate the test cases in this study, which comprise of 3 porous cases (C39, C64, and C133), covering a range of $0.1 \lesssim \phi \lesssim 0.33$ ($2.5 \lesssim aD \lesssim 8.5$, where a is the frontal area per unit volume, $a \equiv N_c d / (0.25 \phi D^2)$), and a solid obstruction case ‘CS’ (figure 1e,

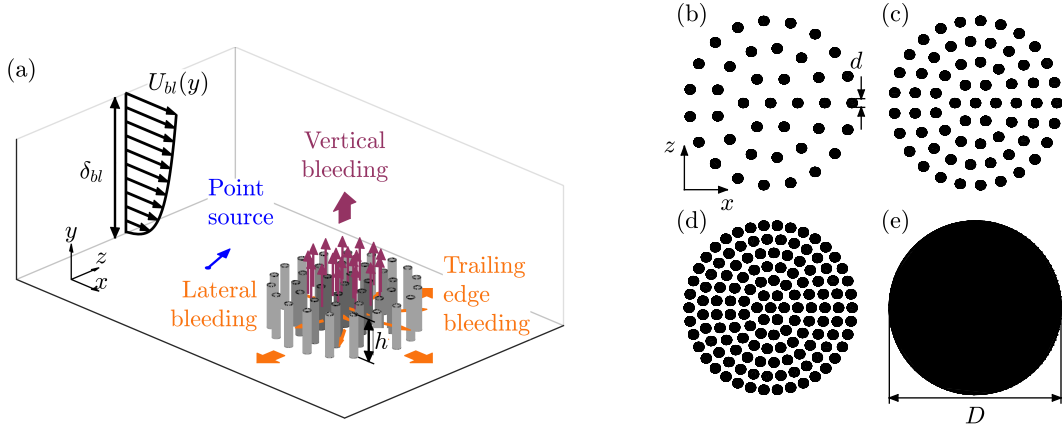


Figure 1. (a) Illustrations of lateral, trailing edge, and vertical bleeding of a porous obstruction. U_{bl} is the incoming boundary-layer velocity, whose thickness is δ_{bl} , and h is the height of the cylinders. Blue arrow shows the location of the point source (fluorescent dye entry point). Illustration of cylindrical array test cases: (b) C39 ($\phi = 0.098$), (c) C64 ($\phi = 0.160$), (d) C133 ($\phi = 0.333$), and (e) the solid case (CS, $\phi = 1$) in x - z plane (top view), d is cylinder diameter and D is the circular patch diameter.

Table 1. List of cylindrical array test cases.

Cases	N_c	d/D	ϕ	aD
C39	39	0.05	0.098	2.483
C64	64	0.05	0.160	4.074
C133	133	0.05	0.333	8.467
CS	1	1	1	1.273

$\phi = 1$).

PIV-PLIF measurements are conducted in the streamwise-wall-normal (x - y) plane, slicing the center-line of the circular patch. The measurement domain is created by combining successive experiments in 3 field-of-views (FOVs), extending downstream of the patch. As many as 3000 PIV image pairs are recorded for each test case in table 1 by two 4 MP CMOS cameras, while a 5.5 MP 16-bit sCMOS camera simultaneously records PLIF images at the rate of 4 Hz (boundary-layer turnover $TU_\infty/\delta_{bl} = 1.4$). The PIV cameras are equipped with wavelength filters to filter out the PLIF signal, and vice versa for the PLIF camera. Image cross-correlation and post-processing of the resulting vectors are performed using a commercial software (DaVis, LaVision GmbH), which gives the spatial resolution of $\Delta x^+ \times \Delta y^+ = 15 \times 15$ ('+' denotes viscous scaling). The total size of the measurement domain is approximately $6.89D \times 4h$ ($x \times y$), which is stitched from 3 FOVs of the size of $2.5D \times 4h$. The complete description of the experimental setup is given in Appendix A of Wangsawijaya *et al.* (2022). Further details of the PLIF calibration technique and image post-processing are given by Vanderwel & Tavoularis (2014) and Lim *et al.* (2022).

TIME-AVERAGED FLOW FIELDS

Figure 2 shows the coloured contours of time-averaged streamwise velocity U for the test cases listed in table 1. Here, the origin $x = 0$ is at the centre of the patch, $y = 0$ on the floor of the tunnel, and U is normalised by $U_{h/2}$ (the incoming velocity at half-height of the cylinder, $y = h/2$). Both porous (figure 2a–c) and solid canopies (figure 2d) show the formation of wake in the form of velocity deficit downstream of the patch.

Recirculation bubbles, here shown by $U < 0$ (blue-shaded contours), appear to be a function of ϕ . In case C64 ($\phi = 0.16$, figure 2b), a weak bubble appears downstream of the patch; it moves upstream towards the patch TE and becomes stronger in case C133 ($\phi = 0.33$, figure 2c). The “delay” in the appearance of recirculation bubble has been previously observed in both 2-D and 3-D patches (Chang & Constantinescu, 2015; Taddei *et al.*, 2016; Zhou & Venayagamoorthy, 2019), and also porous plates (Castro, 1971).

Superimposed on the contours of U in figure 2 are the line contours of the Reynolds shear stress $-\overline{u'v'}/U_{h/2}^2$ (solid black lines). The contours show the formation of a free shear layer (or a mixing layer) downstream of the patch, as the wake of the patch comes into contact with the undisturbed, faster flow in the freestream (Nicolai *et al.*, 2020). Meanwhile, the region below the layer and downstream of the patch TE is shielded from mixing. The magnitude of $-\overline{u'v'}$ increases with ϕ , with a similar pattern observed in the variances $\overline{u'u'}$ and $\overline{v'v'}$ (not shown for brevity). The layer appears to be lifted off the patch as ϕ increases for the porous patches in figure 2(a–c), which is attributed to vertical bleeding from the interior of the patches. Although the magnitude of the shear stress is higher, the lift-off is not observed in the solid case CS (figure 2d) as the flow is not able to escape vertically from the patch in this case.

The time-averaged scalar field normalised by its concentration at the point source C/C_s (shown in solid gray lines in figure 2 and coloured contours in figure 3) allows further examination of the flow; with this aim, only high values of mean concentration are shown in figure 2: the most external contour refers to a value of 1×10^{-3} . In case C39 (figure 2a), no recirculation is observed and high magnitude of C is apparent downstream of the patch as the flow bleeds from the TE. As ϕ increases in case C64 (figure 2b), the region of high C is trapped by a recirculation bubble (blue-shaded contours) downstream of this region. At the highest ϕ (case C133, figure 2c), recirculation is observed at the TE and largely preventing TE bleeding from the patch as well as scalar penetration downstream of the patch (no contour lines downstream of the patch compared to cases C39 and C64), followed by higher C above the patch ($0 \leq x/D \leq 0.5$, $y/h > 1$), which signals a stronger vertical bleeding. The magnitude of C above the patch is proportional to ϕ , which also coincides with the elevation of the shear layer (coloured contours in figure 3, cf. solid black lines in figure 2). For porous obstructions such as these,

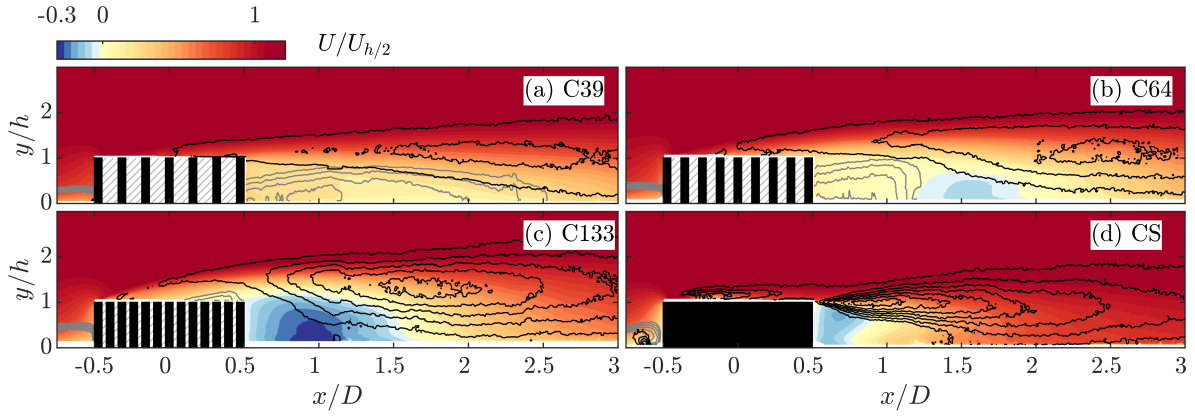


Figure 2. Contours of time-averaged streamwise velocity $U/U_{h/2}$ of case: (a) C39, (b) C64, (c) C133, and (d) CS. Solid black lines (—) are the Reynolds shear stress $-\overline{u'v'}/U_{h/2}^2$ with the following contour levels: 0.4, 1, 1.6, ..., 4×10^{-2} . Solid gray lines (—) are the time-averaged scalar concentration in logarithmic scale $\log_{10}(C/C_s)$ with the following contour levels: $-3, -2.9, \dots, -2.5$. Measurement data are not available in the hatched regions.

TE bleeding is limited by the recirculation bubble. From the flow's perspective, the patch appears to be 'extended' downstream, with the length of the extension inversely proportional to ϕ (possibly akin to the length of "steady wake region" observed by Ball *et al.* (1996); Chen *et al.* (2012); Zong & Nepf (2012)). As ϕ increases, the shear layer is elevated upward, shielding the high C region above the patch and limits the vertical bleeding from the interior of the patch. The net effect is the 'taller' appearance of the patch. Further investigation of the time-averaged flow fields is detailed in Wangsawijaya *et al.* (2022).

ADVECTIVE VERTICAL SCALAR TRANSPORT

Figure 3 shows the coloured contours of C/C_s , superimposed with the line contours of normalised time-averaged wall-normal velocity $V/U_{h/2}$. For the porous patches (figure 3a–c), the previous observation regarding the time-averaged vertical bleeding is further confirmed by the high magnitude of $V > 0$ above the patch, which increases with patch density ϕ . For the solid patch (case CS figure 3d), a strong updraft ($V > 0$) is observed in at leading edge of the patch due to flow separation rather than vertical bleeding, followed by a downdraft ($V < 0$, solid gray lines in figure 3d) downstream of this region.

The strong updraft observed in the porous patches due to vertical bleeding (figure 3a–c) coincides with coincides with increasing vertical penetration of the scalar above the patch, which increases further with ϕ . At the TE of the patch, high magnitude of C at lower ϕ (figure 3a,b) coincides with relatively low magnitude of V . As ϕ increases, however, a strong updraft appears at the TE of the patch ($0.5 \leq x/D \lesssim 1$, figure 3c,d), coinciding with lower magnitude of C compared to that of figure 3(a,b). This results in a highly positive advective scalar flux (upward transport of the mean scalar, $CV > 0$) in the region surrounding the patch: above and at the TE of the patch, with the magnitude of CV increases with ϕ .

TURBULENT VERTICAL SCALAR TRANSPORT

Figure 4 shows the contours of turbulent vertical scalar flux $\overline{c'v'}$ for all porous and solid cases. The contours are normalised by the source concentration C_s and the velocity at half-height of the cylinders $U_{h/2}$. The contours show a largely positive $\overline{c'v'}$ regions, i.e. the layer grows above the patch and

diverges downstream of the patch. The development of $\overline{c'v'}$ layer is similar to that of the shear layer (shown by the line contours of $u'v'$ in figure 2), and thus related to the vertical exchange of scalar inside the shear layer. For the porous cases, the magnitude of $\overline{c'v'}$ is also proportional to ϕ . The exception to this is the solid case CS, which has a relatively lower $\overline{c'v'}$ but higher $-\overline{u'v'}$ compared to that of the porous cases (cf. figure 2d and 4d). Similar pattern in the development of turbulent scalar flux and the "rooftop" shear layer has been observed in various models of urban topography (Tomas *et al.*, 2017; Herwig *et al.*, 2019; Lim *et al.*, 2022).

It is noted that the high magnitudes of the advective and turbulent terms, CV and $\overline{c'v'}$, respectively, occur in different regions of the flow fields. High magnitude of CV is concentrated around the patch; it is observed between the patch and the shear layer ($1 < y/h \lesssim 1.5$, cf. figure 2b,c and 3b,c), and at the TE of the patch up to $x \approx D$ (see figure 3c), where a strong updraft ($V > 0$) coincides with high mean scalar concentration C . Downstream of this region ($x \gtrsim D$), the magnitude of CV decays dramatically, signaling less activity or transport of the scalar by the mean flow. In its place is the region of highly positive $\overline{c'v'}$ (figure 4), which is persistent downstream along with the shear layer.

We further examine the content of the turbulent flow inside the shear layer, which is also the region with high magnitude of $\overline{c'v'}$, by calculating the joint probability density (PDF) of the vertical velocity and scalar fluctuations (from their Reynolds averages), v' and c' , respectively. For each of the porous cases (figure 4a–c), joint PDFs are calculated at two points marked by 'x'. These points are selected by tracing the maximum value of $\overline{c'v'}$ downstream of the patch, $x/D > 0.5$. Where shear layer lift-off is clearly observed (e.g. in case C64 and C133 in figure 4b,c), the location of maximum $\overline{c'v'}$ above high CV region ($y > h$) is selected as the first point (labelled (i) in figure 4b,c). The second point is selected at the maximum $\overline{c'v'}$, downstream of the high CV region (labelled (ii) in figure 4b,c). For the case with lowest ϕ (C39), where shear layer lift-off is not visible, the first point is in the near-wake region ($x/D \approx 0.75$), where high magnitude of $\overline{c'v'}$ is observed, approximately at the half-height of the cylinders (labelled (i) in figure 4a). The second point (labelled (ii) in figure 2a) coincides with the shear layer (figure 2a) further downstream of point (i). For the solid case CS, there is no vertical bleeding; the joint PDF is calculated at the location of maximum $\overline{c'v'}$

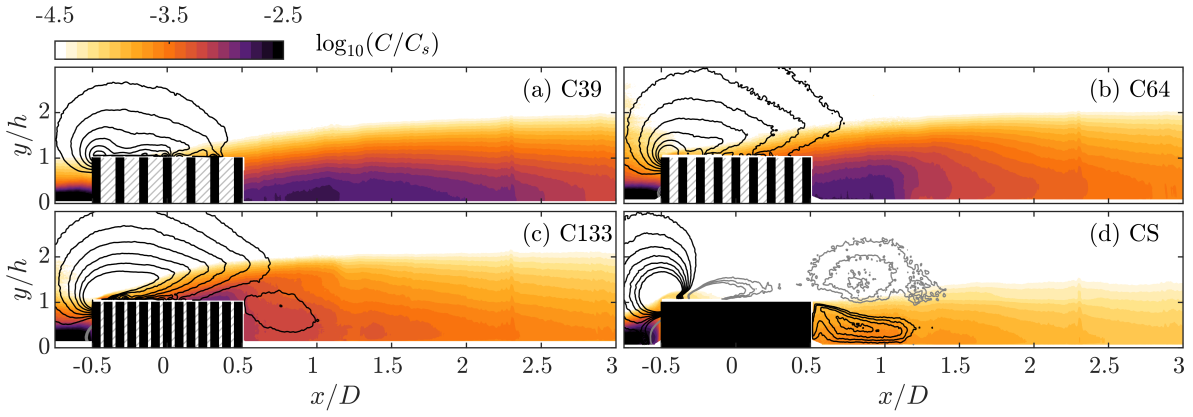


Figure 3. Contours of time-averaged scalar concentration in logarithmic scale $\log_{10}(C/C_s)$ of case: (a) C39, (b) C64, (c) C133, and (d) CS. Solid lines are the time-averaged wall-normal velocity $V/U_{h/2}$ with the following contour levels: 0.05, 0.075, ..., 0.2 (—) and $-0.08, -0.07, -0.06$ (---). Measurement data are not available in the hatched regions.

downstream of the patch (labelled (i) in figure 4d), underneath the shear layer (figure 2d).

Figure 4(a)(i) shows the joint PDF of c' and v' of case C39 (lowest ϕ) at the location marked by ‘i’ in figure 4(a). This location coincides with the region with higher magnitude of C (and thus CV , figure 2a and 3a) due to flow bleeding from the interior of the patch towards the TE. The joint PDF shows a relatively equally distributed probability of c' and v' events across all four quadrants, with a slightly higher probability of $c' < 0$ event. However, as ϕ increases in case C64 and C133, the joint PDFs shown in figures 4(b)(i) and (c)(i) are highly skewed towards Q1 and Q3 events ($c' > 0$ accompanied with $v' > 0$ and $c' < 0$ accompanied with $v' < 0$), with higher probability of Q3 event. This location coincides with the elevated shear layer (figure 2b,c), below the region of high CV magnitude (strong updraft and/or high scalar concentration). The high probability of Q3 event ($c' < 0$ and $v' < 0$) is related to the entrainment of turbulent flow from the shear layer, where enhanced turbulent scalar transport occurs, towards the region shielded below by this layer. Downstream of the high CV region, shear layer develops and diverges further (figure 2a–c). Joint PDFs at this location for all porous cases (figure 4a(ii)–c(ii)) show the same pattern as that of point (i), although with less skewness towards Q1 and Q3. For all porous cases, mixing and entrainment of the turbulent flow towards the wake depend on ϕ ; the strength of the shear layer (figure 2) and the skewness of c' and v' towards Q3 events grow with increasing ϕ . The higher probability of Q3 events ($c' < 0$ rather than $c' > 0$) is related to the diffusivity of the scalar, as the scalar is more likely to be transported to different locations (in this case entrained to the wake below the shear layer, $v' < 0$ event). However, we also note that the magnitude of $c' < 0$ seems to be limited to a certain value (figure 4b(i),c(i)), possibly caused by post-processing of the PLIF image, which will be examined in the future. Examination of joint PDFs of c' and u' at the same location inside the shear layer (figure 4b(iii) and c(iii)) shows that the probability is highly skewed towards Q2 ($c' < 0, u' > 0$) and Q4 ($c' > 0, u' < 0$) events, with higher probability of Q2 ($c' < 0$ accompanied by $u' > 0$), which can be translated as the scalar diffuses further downstream of the patch. As the shear layer diverges (figure 4b(iv) and c(iv)), the skewness towards Q2 and Q4 persists, although there is an increasing possibility of Q3 events ($u' < 0$, slower flow) as this point is located just downstream of the recirculation regions ($U < 0$, figure 2b,c).

In the solid case CS, joint PDF calculated at the maxima

of $\overline{c'v'}$ (figure 4d(i)) is highly skewed towards $c' < 0$ but shows neither preference towards $v' > 0$ nor $v' < 0$. In this case, there is neither vertical bleeding nor TE bleeding as the flow is unable to escape from the interior of the patch. Instead, the flow separates at the top and the sides of the patch. As the wake sheds from the sides of the patch, there are two possible interpretations of $c' < 0$ event: either the scalar has been transported to other in-plane locations, or out of the plane. To examine these possibilities further, figure 4(d)(iii) show the joint PDF of c' and u' calculated at the same location marked by ‘x’ in figure 4(d). The joint PDF of c' and u' shows a similar pattern to that of c' and v' . There is no clear preference towards $u' < 0$ or $u' > 0$, but there is a high probability towards $c' < 0$. This suggests that for the solid case CS, wake shedding from the sides of the patch is more likely to transport the scalar out of the plane.

CONCLUSIONS

We conduct simultaneous PIV-PLIF measurements of flow around a cluster of cylinders on a circular patch, over a range of canopy density ϕ . Present results suggest that both vertical and TE bleeding from the interior of the cylinders, wake formation, shear/mixing layer development, scalar concentration, and vertical scalar transport (both advective and turbulent) are dependent upon ϕ . In terms of TE bleeding and wake formation downstream of the patch, recirculation bubble is shifted downstream as ϕ decreases, limiting the flow from convecting downstream. As ϕ increases, the recirculation bubble appears at the TE of the patch, forcing the flow to bleed vertically from the patch; this results in the elevation of the free shear layer developing above and downstream of the patch. The net effect is the appearance of “taller” canopy as ϕ increases and “elongated” as ϕ decreases.

In terms of scalar transport, results suggest that both advective and turbulent vertical scalar fluxes (CV and $\overline{c'v'}$, respectively) are enhanced as ϕ increases. High magnitude of CV is detected around the patch, where the flow bleeds vertically from the interior of the patch towards the freestream and from the TE of the patch. On the other hand, the occurrence of high magnitude of turbulent vertical scalar flux $\overline{c'v'}$ largely coincides with the shear layer. Further analysis of the joint PDF of c' and v' suggests that inside the shear layer, mixing is enhanced (and more so as ϕ increases), there is an entrainment of turbulent flows from this layer towards the wake region forming below this layer, followed by scalar diffusion towards the

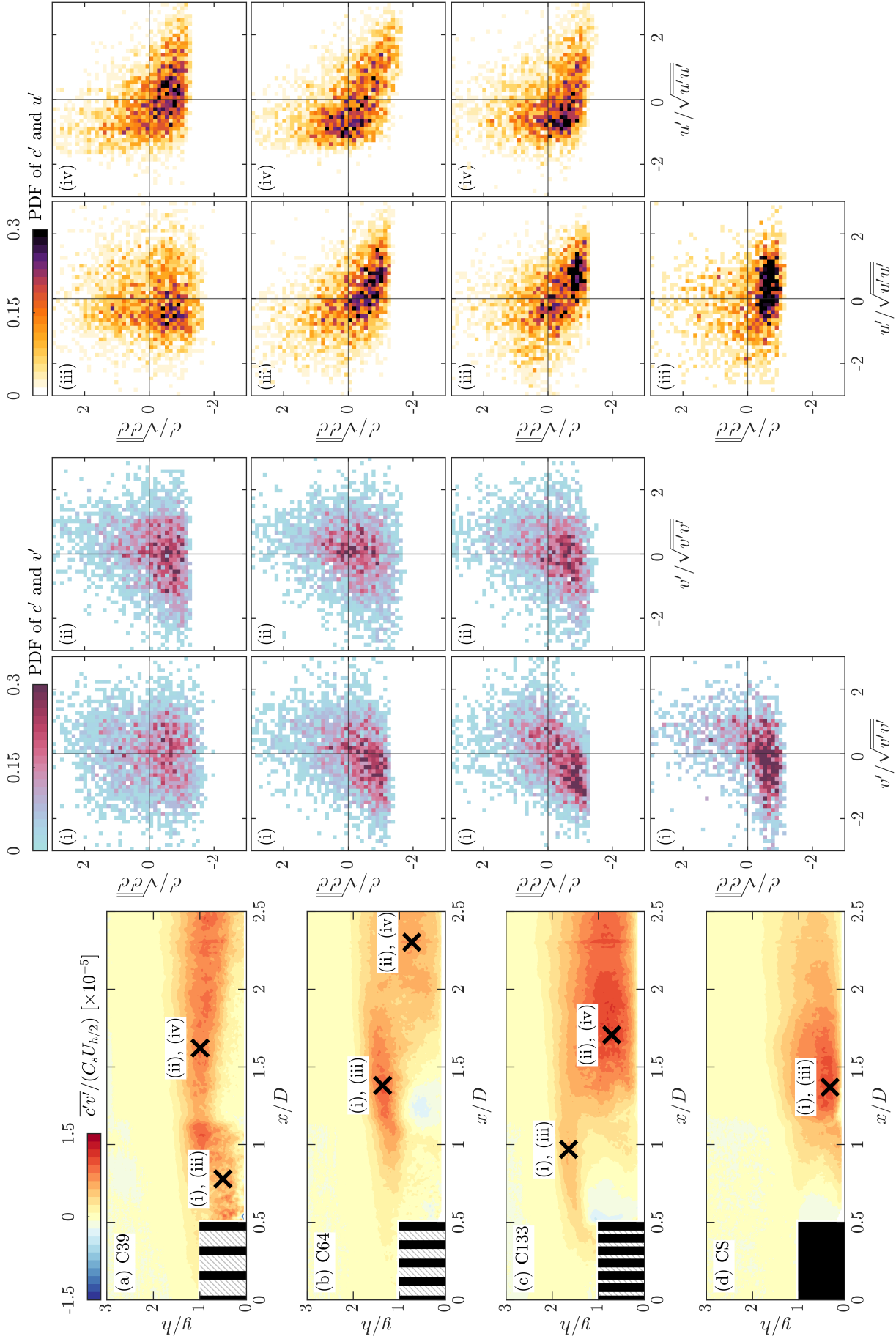


Figure 4. (a–d) Contours of turbulent vertical scalar flux $\overline{c'v'}$, normalised by $C_s U_{h/2}$ for all test cases shown in table 1. ‘X’ denote the location where joint PDF of c' and v' is calculated from each instantaneous velocity and scalar concentration fields. The joint PDFs, corresponding to locations (i, iii) and (ii, iv), are shown to the right of the $\overline{c'v'}$ contours of each test case. Plots (i) and (ii) correspond to the vertical velocity and scalar fluctuations, v' and c' , normalised by their respective root mean square, $\sqrt{v'v'}$ and $\sqrt{c'c'}$, while plots (iii) and (iv) correspond to the streamwise velocity and scalar fluctuations, u' and c' .

same direction and further downstream of the patch. For the solid case CS, however, where there is neither vertical nor TE bleeding, it is more likely for the scalar to be transported out of the PIV-PLIF plane.

REFERENCES

- Ball, DJ, Stansby, PK & Allison, N 1996 Modelling shallow water flow around pile groups. *Proc. Instn Civ. Engrs Wat., Marit. & Energy* **118** (4), 226–236.
- Castro, IP 1971 Wake characteristics of two-dimensional perforated plates normal to an air-stream. *J. Fluid Mech.* **46** (3), 599–609.
- Chang, K & Constantinescu, G 2015 Numerical investigation of flow and turbulence structure through and around a circular array of rigid cylinders. *J. Fluid Mech.* **776**, 161–199.
- Chen, Z, Ortiz, A, Zong, L & Nepf, H 2012 The wake structure behind a porous obstruction and its implications for deposition near a finite patch of emergent vegetation. *Water Resour. Res.* **48** (9).
- Grimmond, CSB & Oke, TR 1999 Aerodynamic properties of urban areas derived from analysis of surface form. *J. Appl. Meteorol. Climatol.* **38** (9), 1262–1292.
- Hertwig, D, Gough, HL, Grimmond, S, Barlow, JF, Kent, CW, Lin, WE, Robins, AG & Hayden, P 2019 Wake characteristics of tall buildings in a realistic urban canopy. *Bound.-Layer Meteorol.* **172**, 239–270.
- Lim, H. D., Hertwig, D, Grylls, T, Gough, H, van Reeuwijk, M, Grimmond, S & Vanderwel, C 2022 Pollutant dispersion by tall buildings: Laboratory experiments and Large-Eddy Simulation. *Exp. Fluids* **EXIF-D-21-00325**, (in print).
- Nepf, HM 2012 Flow and transport in regions with aquatic vegetation. *Annu. Rev. Fluid Mech.* **44**, 123–142.
- Nicolai, C, Taddei, S, Manes, C & Ganapathisubramani, B 2020 Wakes of wall-bounded turbulent flows past patches of circular cylinders. *J. Fluid Mech.* **892**.
- Nicolle, A & Eames, I 2011 Numerical study of flow through and around a circular array of cylinders. *J. Fluid Mech.* **679**, 1–31.
- Taddei, S, Manes, C & Ganapathisubramani, B 2016 Characterisation of drag and wake properties of canopy patches immersed in turbulent boundary layers. *J. Fluid Mech.* **798**, 27–49.
- Tomas, JM, Eisma, HE, Pourquie, MJB, Elsinga, GE, Jonker, HJJ & Westerweel, J 2017 Pollutant dispersion in boundary layers exposed to rural-to-urban transitions: Varying the spanwise length scale of the roughness. *Bound.-Layer Meteorol.* **163**, 225–251.
- Vanderwel, C & Tavoularis, S 2014 On the accuracy of PLIF measurements in slender plumes. *Exp. Fluids* **55** (8), 1–16.
- Wangsawijaya, DD, Nicolai, C & Ganapathisubramani, B 2022 Time-averaged velocity and scalar fields of the flow over and around a group of cylinders: A model experiment for canopy flows. *Flow* **2**.
- Zhou, J & Venayagamoorthy, SK 2019 Near-field mean flow dynamics of a cylindrical canopy patch suspended in deep water. *J. Fluid Mech.* **858**, 634–655.
- Zong, L & Nepf, H 2012 Vortex development behind a finite porous obstruction in a channel. *J. Fluid Mech.* **691**, 368–391.